I. J. Trans. Phenomena, Vol. 15, pp. 37–52
Reprints available directly from the publisher
Photocopying permitted by license only

Numerical Analysis of the Influence of Low Frequency Vibration on Bubble Growth

D. HAN[1,*] AND MARK A. KEDZIERSKI[2]

[1]*Institute of Advanced Machinery Design Seongbuk-Gu, Seoul, 136-701, South Korea*
[2]*National Institute of Standards and Technology Gaithersburg, MD 20899, USA*

Numerical simulation of bubble growth during pool boiling under the influence of low frequency vibration was performed to understand the influence of common vibrations such as those induced by wind, highway transportation, and nearby mechanical devices on the performance of thermal systems that rely on boiling. The simulations were done for saturated R123 boiling at 277.6 K with a 15 K wall superheat. The numerical volume-of-fluid method (fixed grid) was used to define the liquid-vapor interface. The basic bubble growth characteristics including the bubble departure diameter and the bubble departure time were determined as a function of the bubble contact angle (20°–80°), the vibration displacement (10 μm–50 μm), the vibration frequency (5 Hz–25 Hz), and the initial vibration direction (positive or negative). The bubble parameters were shown to be strongly dependent on the bubble contact angle at the surface. For example, both the bubble departure diameter and the bubble departure time increased with the contact angle. At the same vibration frequency and the initial vibration direction, the bubble departure diameter and the bubble departure time both decreased with increasing vibration displacement. In addition, the vibration frequency had a greater effect on the bubble growth characteristics than did the vibration displacement. The vibration frequency effect was strongly influenced by the initial vibration direction. The pressure contour, the volume fraction of vapor phase, the temperature profile, and the velocity vector were investigated to understand these dynamic bubble behaviors. The limitation of the computational fluid dynamics approach was also described.

Keywords: Bubble departure diameter, bubble departure time, CFD, pool boiling, vibration, VOF

INTRODUCTION

It is common for heat transfer devices to be exposed to various kinds of vibration that originate from nearby mechanical devices, road traffic, incident wind, and other vibrations that transmit through foundations. Vehicular traffic produces vibration frequencies between 5 Hz and 25 Hz (Hunaidi, 2000). Consequently, the need to understand the effect of vehicular traffic vibrations on the performance of heat transfer equipment has led to

*Corresponding author: E-mail: microfin718@gmail.com; Tel./fax: +82-2-928-2170 /+82-2-928-2171

several recent investigations near this frequency range. For example, the effect of simulated road vibration (30 Hz–150 Hz, 3g acceleration) on fuel cell efficiency was investigated by Hou et al. (2013). They found that all of the key performance factors of a fuel cell were negatively affected by vibration, including a 56% increase in ohmic resistance. Prisniakov et al. (2002) measured the thermal performance of heat pipes while applying 10 Hz–100 Hz frequencies of 3 μm–5 μm displacements and found that the heat transfer coefficients were increased by as much as 5% to 30%.

Ultrasonic acoustic vibration has been intentionally used to augment boiling heat transfer by causing cavitation (Legay et al., 2011) and fluid streaming (Riley, 1998). In addition, nanofluids boiling can be acoustically enhanced via increased interaction between nanoparticles and bubbles (Kedzierski and Fick, 2014). However, cavitation is the most prevalent heat transfer augmentation mechanism, which acts by mixing the boundary layer by bubble implosion. This mechanism also aids in bubble removal, growth, creation and agitation. Similarly, acoustic streaming also enhances fluid mixing by inducing a jet of convecting bubbles. These mechanisms also delay the onset of film boiling, thus, allowing for higher critical heat fluxes.

As far as pool boiling is concerned, there are few studies that are applicable to the road vibration frequency range. For example, all of the acoustically enhanced boiling studies reviewed by Legay et al. (2011) were for excitation frequencies mostly beyond road vibrations, i.e., between 15 kHz and 60 kHz. For this frequency range, Legay et al. (2011) were able to show some heat transfer benefit for each study. In contrast, for a vibration frequency closer to road vibration, i.e., for 80 Hz, Prisniakov and Prisniakov (1997) showed a decrease in the pool boiling bubble frequency and corresponding heat transfer. The bubble frequency was degraded as much as 40% as compared to that for no vibration. The degradation was also found to be dependent on the amplitude of the vibration. The effect of vibration frequency and amplitude on pool boiling is significant and variable. Consequently, more pool boiling studies in the lower frequency range, which are applicable to road vibrations, are needed to better understand this phenomenon.

The study of fundamental bubble growth mechanisms, as altered by vibration, is critical to understanding the thermal behavior of heat transfer systems in real-world environments. Key parameters of interest for pool boiling are the bubble departure diameter and the bubble departure frequency. High speed imaging has formed the basis of numerous prediction models for these bubble parameters. However, the experimental visualization of bubbles is expensive and difficult to conduct. In addition, experimentally isolating single bubbles for study for determining the bubble departure diameter and bubble departure frequency is problematic due to their small size and short time scale. A numerical analysis has advantages over an experimental method because it does not suffer from these difficulties. As a result, a relatively large number of computational fluid dynamics approaches have been carried out to study boiling phenomenon. For example, Esmaeeli and Tryggvason (2004a, b) extended their work from single bubble to multiple bubbles into the film boiling region. Son and Dhir (2008) simulated three dimensional film boiling on a horizontal cylinder. Welch and Wilson (2000) and Sun et al. (2000) used the volume-of-fluid (VOF) method to numerically analyze film boiling. Like these, most studies are restricted to film boiling, which is not a desired operational design condition for most heat exchangers. For this reason, the pool boiling bubble behavior under low frequency vibration is investigated with the assistance of computational numerical analysis while varying the bubble contact angle, the vibration frequency, the vibration displacement, and the initial vibration direction.

NUMERICAL ANALYSIS

The numerical analysis for two-dimensional two-phase flow was done using the volume-of-fluid (VOF) method of the ANSYS FLUENT®[†] software, which is convenient for analyzing the dynamic characteristics of the liquid-vapor interface near the heating surface. The VOF model is the pressure based solver and valid for mixtures of immiscible fluids. It solves a single set of momentum equations and traces the volume fraction of

[†] Certain trade names and company products are mentioned in the text or identified in an illustration in order to adequately specify the simulation procedure. In no case does such an identification imply recommendation or endorsement by the National Institute of Standards and Technology (NIST), nor does it imply that the products are necessarily the best available for the purpose.

each fluid. It is typically adapted for a time dependent modeling and assumes that fluids are not interpenetrating. The tracking of the phase interface is achieved by solving the volume fraction continuity equation.

The grid size that is sufficient for capturing the liquid-vapor interface dynamics was determined by varying the grid density until the results became independent of the size of the grid. After the grid independency check, the bubble contact angle that produced the correct bubble departure diameter for a particular frequency was determined by trial and error.

The following assumptions were applied to the numerical model:

- Incompressible g\aseous phase: The considered working fluid, R123, is a relatively low pressure refrigerant with a saturation pressure of 39.85 kPa at 277.6 K.
- Laminar flow: The boiling phenomenon was restricted to pool boiling without the influence of forced convection.
- Newtonian flow and constant fluid properties: The FLUENT® solver was divergent with temperature dependent properties. Therefore, constant fluid properties were used.
- No-slip boundary conditions at the fluid-solid interfaces.
- No cavitation.
- Vibration forces are aligned along the same axis as gravity forces.
- The simulated range of external frequency is far lower than the resonance frequency of a bubble. The considered vibration frequency was less than 25 Hz which is much lower than the resonance frequency of a bubble (Prosperetti, 1988).
- No lubricant: Foaming and lubricant rich layer by selective evaporation were not considered.
- No interaction with nearby nucleate sites: The simulation is restricted to single bubble behavior.

Governing Equations

The VOF model was used to investigate the boiling behavior near a heated surface because of its appropriateness for immiscible liquid-vapor transient flow. In the VOF model, the sum of the fractions in each phase is unity in a cell and the local cell properties in the transport equations are determined based on the present volume fraction of each phase. A property (Π), e.g., viscosity, density, and thermal conductivity, in each cell was linearly weighted with the vapor void fraction (α):

$$\prod = \alpha \prod_{v} + (1-\alpha) \prod_{liq} \tag{1}$$

The volume fraction equation can be expressed as

$$\left[\frac{\partial}{\partial t}(\alpha_i \rho_i) + \nabla \cdot (\alpha_i \rho_i \vec{v}_l)\right] = \dot{m}_i \tag{2}$$

Where the density of the fluid and the vibrational velocity at the interface are ρ_i and v_i, respectively. The vibration velocity has a linear relationship with the vibration displacement and the vibration frequency ($v_i = A\omega\cos\omega t$). Here, ω is the angular frequency ($\omega = 2\pi f$) and t is time.

The m_i is the interfacial mass transfer rate per volume and can be obtained as:

$$\dot{m}_i = -\frac{(k_v \alpha_v + k_{liq}(1-\alpha_v)(\nabla T \cdot \nabla \alpha_{liq})}{i_{lg}} \tag{3}$$

The k_v and k_{liq} are the thermal conductivity of the vapor and the liquid, respectively, while i_{lg} is the latent heat of vaporization. In addition, A_b is the surface area of bubble. Because there is no internal mass source, the mass source for the liquid phase becomes:

$$\dot{m}_{liq} = -\dot{m}_i \tag{4}$$

The pertinent momentum equation has the following form.

$$\frac{\partial}{\partial t}(\rho \vec{v}) + \nabla \cdot (\rho \vec{v} \vec{v}) = -\nabla_p + \nabla \cdot [\mu(\nabla \vec{v} + \nabla \vec{v}^T)] + \rho \vec{g} + \vec{F} \tag{5}$$

where F is a function of surface tension, the surface curvature, and the volume fraction gradient (Brackbill et al., 1992).

The energy equation can be written as:

$$\frac{\partial}{\partial t}(\rho i) + \nabla \cdot (\rho \vec{v} i) = \nabla \cdot [k(\nabla T)] \pm \dot{m}_v i_{lg} \tag{6}$$

where the average enthalpy is:

$$i = \frac{\alpha \rho_v i_v + (1-\alpha)\rho_{liq} i_{liq}}{\alpha \rho_v + (1-\alpha)\rho_{liq}} \tag{7}$$

and $\dot{m}_v i_{lg}$ is positive for the vapor side and negative for the liquid side.

The first order implicit (Turkel and Vatsa, 2003), PRESTO![‡] (Peyret, 1996), and QUICK (Leonard and Mokhatari, 1990) schemes were used for the discretization of time, pressure, and momentum, respectively. For pressure-velocity coupling, the PISO scheme was adapted. In the implicit equation, the unknown values in a cell were calculated using known and unknown values from neighboring cells and a scalar transport equation was solved iteratively for the liquid-phase volume fraction at each time step. The implicit scheme was selected because it allows for large time steps as compared to the explicit scheme. The PRESTO! scheme was selected because it is suitable for steep pressure gradients. This scheme uses the discrete continuity balance for a staggered control volume to calculate the pressure. The QUICK scheme is based on a weighted average of the second order upwind and the central interpolations of the variable. The PISO (Pressure-Implicit with Splitting of Operators) scheme is based on higher degree approximations for the pressure and the velocity corrections, which improves the calculation efficiency for the momentum balance by using both the neighbor correction (Issa, 1985) and the skewness correction (Ferzieger and Peric, 1996).

The dynamic mesh model in FLUENT (2011) was used to model flows in harmonic motion where the location of the domain changes with time due to the motion of the domain. In this way, oscillatory motion may be modeled with an integral form of the conservation equation for a general scalar on an arbitrary control volume with a moving boundary:

$$\frac{d}{dt}\int_v \rho\phi dV + \int_{\partial v} \rho\phi(\vec{u}-\vec{u}_m)\cdot d\vec{A} = \int_{\partial v}\Gamma\nabla\phi\cdot d\vec{A} + \int_v S_\phi dV \tag{8}$$

where dV represent the boundary of the control volume, V, $\vec{u}_m$ is the velocity of the moving mesh, Γ is the diffusion coefficient, and S_ϕ is the source term of the general scalar ϕ. The 2nd term of eq. (8) represents conservation of momentum flux through the boundaries of the control volume moving at $\vec{u}_m$.

The influence of the displacement (A), the initial phase (φ), and the angular frequency (ω) of the vibration is imposed on the model via the mesh velocity ($\vec{u}_m$). The mesh velocity has the form of harmonic motion as follows:

$$\vec{u}_m = A\omega\cos(\omega t+\varphi) \tag{9}$$

The mesh velocity parameters strongly influence the magnitude of the acceleration that is applied to the fluid element. The initial phase angle determines the initial moving direction of the whole domain. The direction of the vibration is limited to $\pm x$ (aligned with gravity) considering the symmetry of the numerical domain. Here $+x$ implies zero initial phase, while $-x$ corresponds to 180° initial phase.

Numerical Domain

All simulations were conducted using the saturated properties of R123 at 277.6 K. The wall superheat (T_{wall}–$T_{ref.\ sat}$) was set to a fixed value of 15 K. At this operating condition, the flow regime is pool boiling (Kedzierski and Han, 2006). The entire numerical domain temperature was initialized to 277.6 K before starting the simulation.

Buildings near high traffic roads experience 5 Hz to 25 Hz vibration (Hunaidi, 2000) and building vibration amplitude should not exceed 0.1 g (Sung, 2007). Hence, 5 Hz, 15 Hz, and 25 Hz frequencies were simulated for this study with vibration displacements of 10 μm, 30 μm, 50 μm as shown in Table 1.

The bubble angular resonance frequency can be expressed as (Prosperetti et al., 1988):

$$\omega_0 = \left[\frac{p}{\rho_{liq}p_b^2}\left(\Phi - \frac{2\sigma}{d_b p}\right)\right]^{1/2} \tag{10}$$

where Φ is a function of gas diffusivity and the ratio of specific heats. The frequency range studied in this paper (5 Hz–25 Hz) is much less than the bubble resonance frequency, which is approximately 6 kHz for the present operating conditions.

All simulated conditions are summarized in Table 1. The effect of displacement was evaluated at the same frequency for cases 10, 13, and 14, while the influence of the frequency was investigated at the identical displacement for cases 10, 11, and 12. Additionally, the influence of the initial phase was examined in cases 15, 16, and 17.

[‡] PREssure STaggering Option.

TABLE 1
Numerical cases

Case No	Grid size	Wall superheat	θ	f	A	initial direction (φ)	Acceleration amplitude
1	30 × 90	15 K	80°	N/A	N/A	N/A	0 g
2	45 × 135	15 K	80°	N/A	N/A	N/A	0 g
3	60 × 180	15 K	80°	N/A	N/A	N/A	0 g
4	75 × 225	15 K	80°	N/A	N/A	N/A	0 g
5	90 × 270	15 K	80°	N/A	N/A	N/A	0 g
6	105 × 315	15 K	80°	N/A	N/A	N/A	0 g
7	90 × 270	15 K	20°	N/A	N/A	N/A	0 g
8	90 × 270	15 K	40°	N/A	N/A	N/A	0 g
9	90 × 270	15 K	60°	N/A	N/A	N/A	0 g
10	90 × 270	15 K	60°	25 Hz	50 μm	+x (0°)	0.13 g
11	90 × 270	15 K	60°	15 Hz	50 μm	+x (0°)	0.05 g
12	90 × 270	15 K	60°	5 Hz	50 μm	+x (0°)	0.01 g
13	90 × 270	15 K	60°	25 Hz	30 μm	+x (0°)	0.08 g
14	90 × 270	15 K	60°	25 Hz	10 μm	+x (0°)	0.03 g
15	90 × 270	15 K	60°	25 Hz	50 μm	−x (180°)	0.13 g
16	90 × 270	15 K	60°	15 Hz	50 μm	−x (180°)	0.05 g
17	90 × 270	15 K	60°	5 Hz	50 μm	−x (180°)	0.01 g

Figure 1a shows the base two-dimensional numerical 90 × 270 grid (numerical domain) with its boundary conditions. The VOF model requires square grid elements of uniform size. The left side of the grid (*a*-*o*) was assigned as a constant temperature wall boundary of 292.6 K. The right side of the grid (*b*-*c*) was set as the outlet pressure. The top of the grid (*a*-*b*) is the symmetry boundary and the bottom of the grid (*o*-*c*) is the axis of the bubble. Gravity acts in the *x*-direction. Considering that a bubble can be treated as an axis-symmetric shape, the two-dimensional numerical domain was analyzed permitting a full bubble to be obtained by rotating the solved domain within the cylinder shown in Fig. 1b.

Figure 1b shows the numerical domain as being the surface from the centerline (*o*-*c*) of the bubble to the outer surface of a cylinder (*a*-*b*). The height of the numerical domain (*a*-*o*) was determined as one quarter of the most dangerous two-dimensional Taylor inviscid wave length, λ (Carey, 1992):

$$\lambda = 2\pi\sqrt{\frac{3\sigma}{(\rho_{liq}-\rho_v)g}} \tag{11}$$

Typically, half of λ is used for the film boiling numerical domain (Esmaeeli and Tryggvason, 2004a). The numerical domain height can be verified by using the following correlation by Kutateladze and Gogonin (1979) for the bubble departure diameter, d_d:

$$d_d = \sqrt{\frac{0.19\sigma(1.8+10^5 k_l)^{2/3}}{g(\rho_{liq}-\rho_v)}} \tag{12}$$

where

$$k_l = \left(\frac{\mathrm{Ja}}{\mathrm{Pr}_{liq}}\right)\left\{\left[\frac{g\rho_{liq}(\rho_{liq}-\rho_v)}{\mu_{liq}}\right]\left[\frac{\sigma}{(\rho_{liq}-\rho_v)g}\right]^{3/2}\right\}^{-1} \tag{13}$$

$$\mathrm{Ja} = \frac{(T_{wall}-T_{sat})c_{p,liq}\rho_{liq}}{\rho_v h_{lg}} \tag{14}$$

At the operating condition, λ is 11.87 mm and the estimated bubble departure diameter is 0.887 mm. For the present analysis, the bubble departure diameter was used to estimate the numerical domain height as one fourth of λ rather than half of λ as done in (Esmaeeli

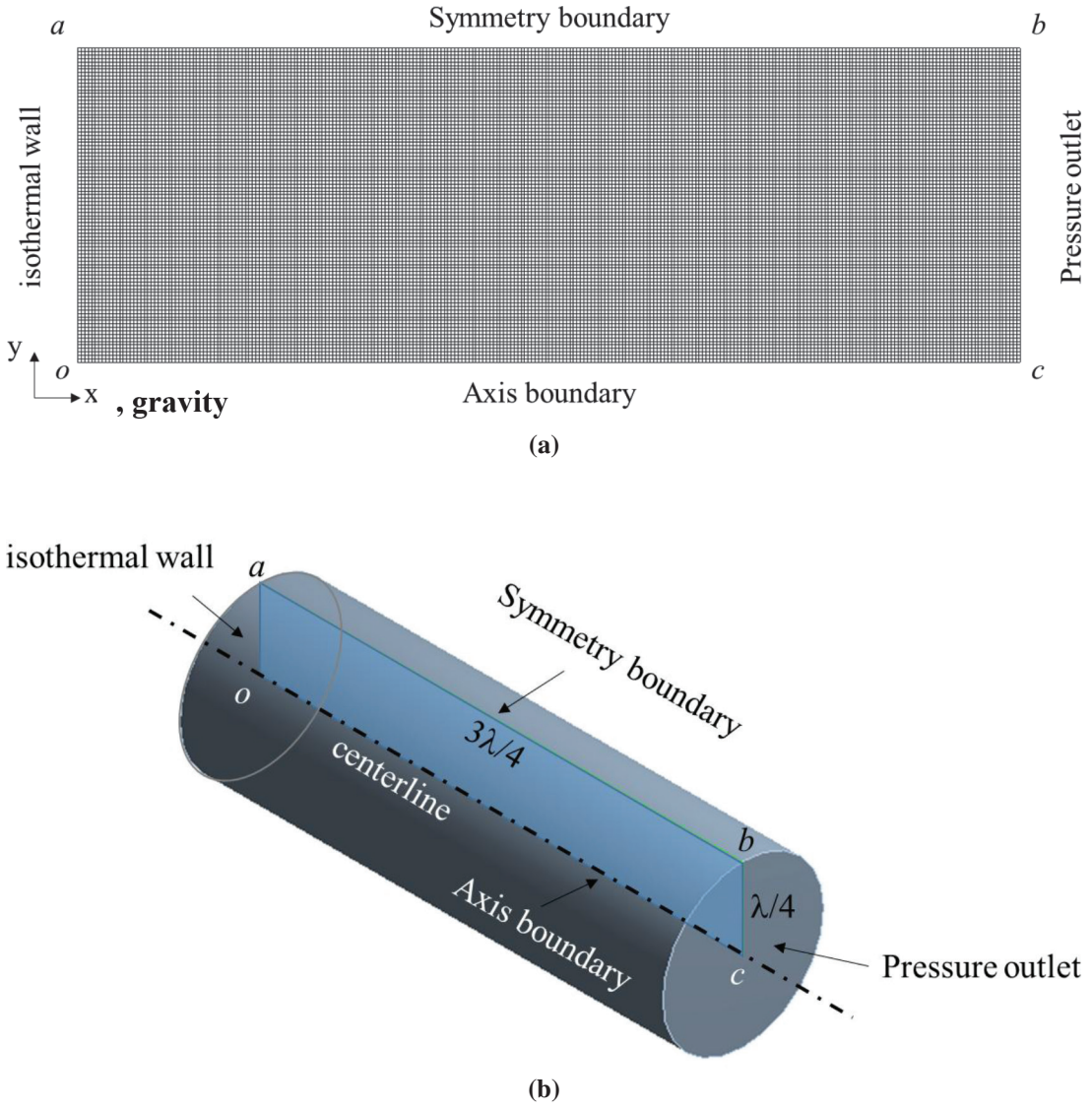

FIGURE 1
Numerical domain. (a) Grid (90 × 270), (b) Conceptual image of the numerical domain (surface inside the cylinder).

and Tryggvason, 2004). For a given contact angle, an embryo bubble having a size of 50% of the bubble diameter predicted by eq. (13) was initially placed in the corner of the axis and the wall boundaries (*a*-*o*-*c*), as shown in Fig. 2.

The length of the numerical domain (*o*-*c*) was estimated as three times the numerical domain height (*a*-*o*). The resultant numerical domain size was 2.966 mm × 8.899 mm.

Time step size was selected as 10^{-4} s by considering the magnitude of the bubble departure frequency, the time scale, and the vibration frequency. Zuber (1959) suggested the following correlation for the product of the bubble frequency (f) and the departure diameter:

$$fd_d = 0.59\left[\frac{\rho_{liq}(\rho_{liq}-\rho_v)g}{\rho_{liq}^2}\right]^{1/4} \tag{15}$$

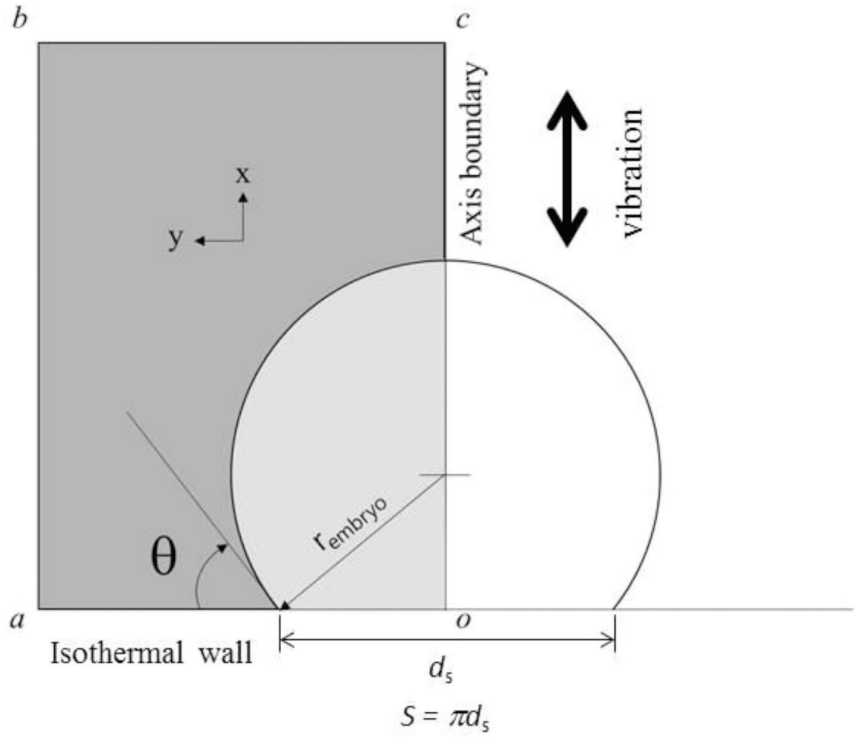

FIGURE 2
Vapor bubble embryo.

The time scale was estimated as:

$$t_s = \left[\frac{\sigma}{(\rho_{liq} - \rho_v)g^3}\right]^{0.25} \tag{16}$$

The bubble departure time and the time scale (t_s) estimated from eqs. (15) and (16) were 0.015 s and 0.011 s, respectively. Considering that the time step size was 10^{-4} s, the simulation had a resolution of approximately 100 time steps and this time step is sufficient to capture the bubble departure time considering the vibration frequency range of this study. The numerical analysis showed that the bubble departure time was 0.047 s for case 9 (base case). Therefore, a bubble was exposed to almost one full cycle of harmonic vibration at the highest frequency of 25 Hz.

The bubble contact angle was set to 80° for the grid size determination process described above. The relative bubble departure diameter and the bubble departure time compared to eqs. (12) and (15) are shown in Fig. 3 as a function of grid density. As illustrated in Fig. 3, the bubble departure diameter and the bubble departure time converged at 60 × 180 and 90 × 270 grids, respectively. Therefore, the 90 × 270 grid was selected for this study. The bubble departure diameter was less sensitive to the choice of grid density than was bubble departure time. For example, as shown in Fig. 3, when the grid was changed from 30 × 90 to 90 × 270 the departure diameter changed by approximately 25% while the departure time changed by approximately 48%.

As Fig. 3 shows, the bubble departure diameter shows good agreement with the prediction model, but a relatively large deviation was observed for the bubble departure frequency compared to the prediction models. This might be expected considering that the adopted correlations were not developed specifically for this operating condition, working fluid, and surface conditions. McHale and Garimella (2010) presented their experimental data of fd_d obtained for a pool boiling regime that showed discrepancies of up to 800% from several existing correlations. To

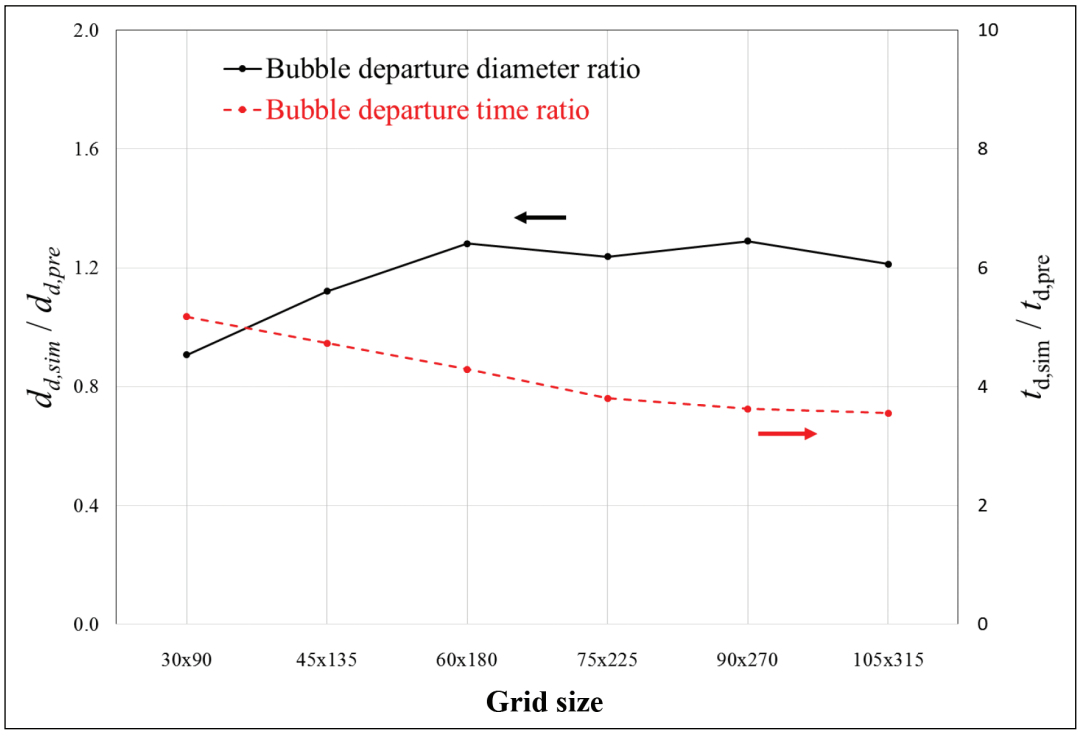

FIGURE 3
Grid dependency.

reduce these differences, the bubble contact angle was varied from 80° to 20° with the selected 90 × 270 grid as shown in Fig. 4. The bubble departure time may be matched to the prediction model (Zuber, 1959) between 40° and 50°. Additional numerical analysis was performed with contact angle of 50°, but the solution did not converge for this case. Hence, the vibration simulations were carried out using an initial dynamic bubble contact angle of 60°. Over the course of the bubble's life, the dynamic bubble contact angle varied between 45° and 60° and its average was approximately 50°, which is larger than what is typically seen for pure refrigerant on a smooth surface. However, Kedzierski (1993) found that reducing the surface energy of a smooth pool boiling surface with the addition of lubricant to R123 increased the average contact angle from 36° for pure R123 to 41° for a 2% by mass mixture of lubricant with R123. A further increase in the contact angle for the R123/lubricant mixture to approximately 50° was achieved by Kedzierski (1993) when forced convection was introduced across the boiling surface. The increase in the contact angle was a consequence of improved bubble removal conditions. The addition of lubricant reduced the bubble wall-attachment forces while the forced convection complimented buoyancy forces in bubble detachment. In a similar way, vibration enhances bubble removal, which is consistent with a larger contact angle than what is typical for pure refrigerant in stagnant pool boiling.

RESULTS

General Bubble Growth Behavior

The bubble departure diameter (d_d) was calculated using the vapor area of the bubble at the moment of departure:

$$d_d = \sqrt{\frac{4A_b}{\pi}} \tag{17}$$

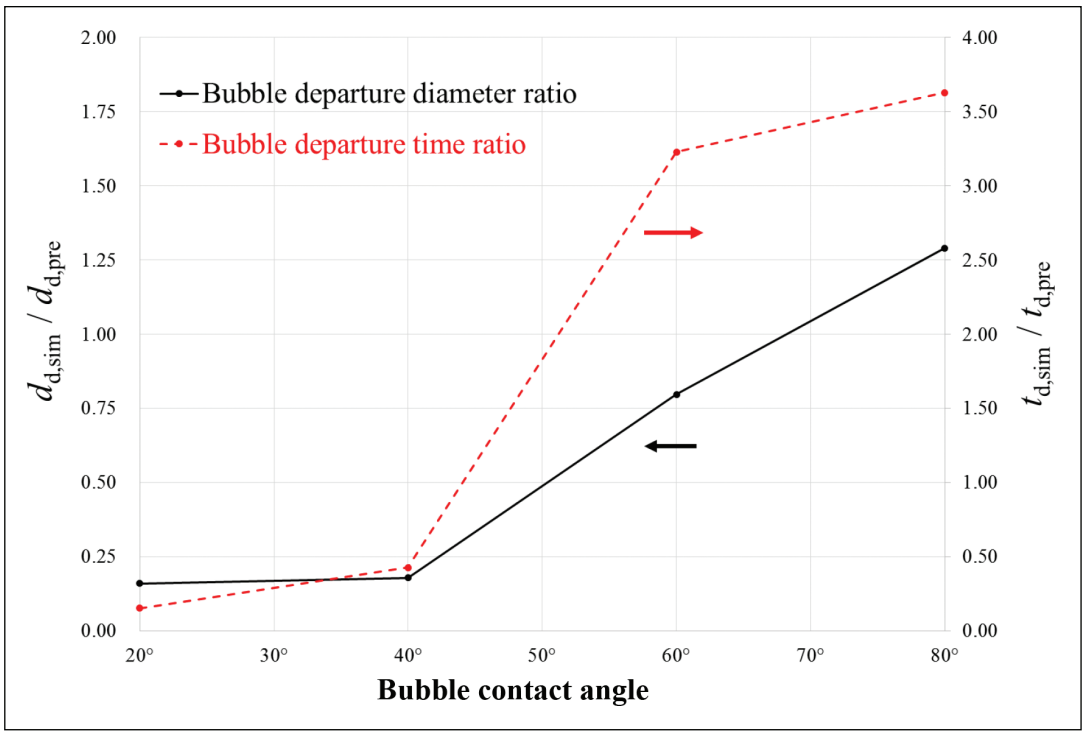

FIGURE 4
The effect of the bubble contact angle.

The bubble departure time is the total required time from bubble incipience to detachment from the surface.

Figure 5 shows the bubble growth dynamics for case 9 (60° bubble contact angle, no-vibration). The velocity vector, the pressure contour, and the temperature contour are also presented together in Fig. 5a. As described above, an embryo bubble grows by heat input through contact with the heated wall which results in a pressure increase inside the bubble. When the bubble reaches the critical volume, the buoyancy force, $gV(\rho_{liq}-\rho_v)$, overcomes the surface tension force, $\sigma S\sin\theta$, and the bubble detaches from the surface. During this process, a small portion of the bubble is separated from the main departing body and left on the heating surface as a vapor seed. Then, the vapor seed starts to grow again. The rising bubble loses its thermal energy quickly to the surrounding liquid and its internal pressure decreases. The velocity field near the bubble is related to the dynamic shape of the bubble. As the enlarged velocity vector profile shows in Fig. 5a, the growth of the bubble induces recirculation of the liquid in a small region near the bubble and the heated wall. When the bubble detaches from the surface and moves upward, the surrounding liquid flows into the layer between the bubble and the wall. The superheated layer near the wall responds closely to the bubble growth while it is attached to the surface and becomes saturated as bulk liquid rushes in to replace the detached bubble.

Figure 5b shows the area weighted average volume fraction as a function of time for an example case. The bubble volume is shown to increase nearly linearly from bubble incipience to bubble departure. The influence of the contact angle on the bubble shape is illustrated by a comparison of Figs. 5, 6, and 7. As shown in the figures, the bubble departure diameter and the bubble departure time increase with the bubble contact angle because a larger bubble volume is required to overcome the increased surface-tension forces.

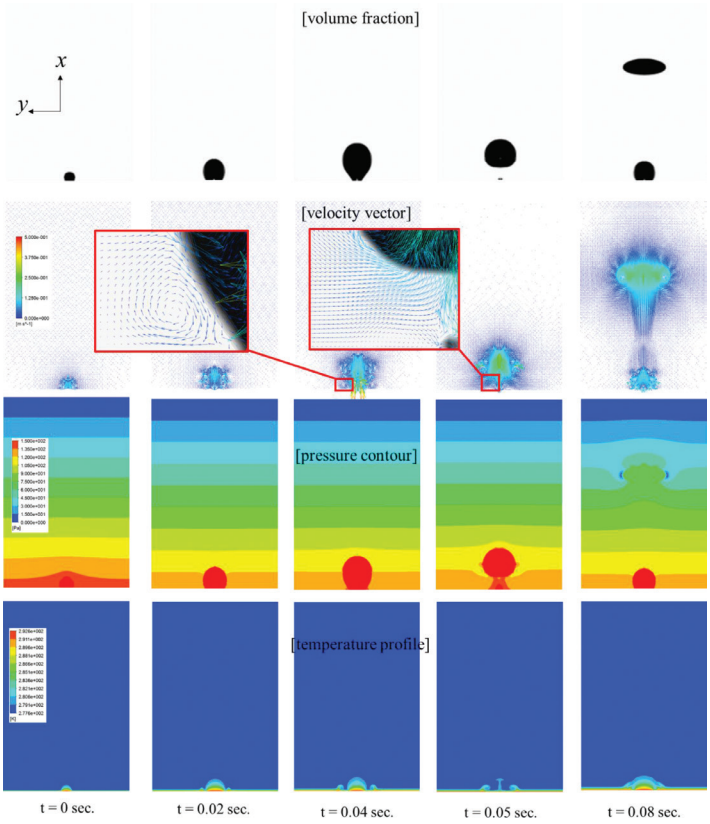

(a)

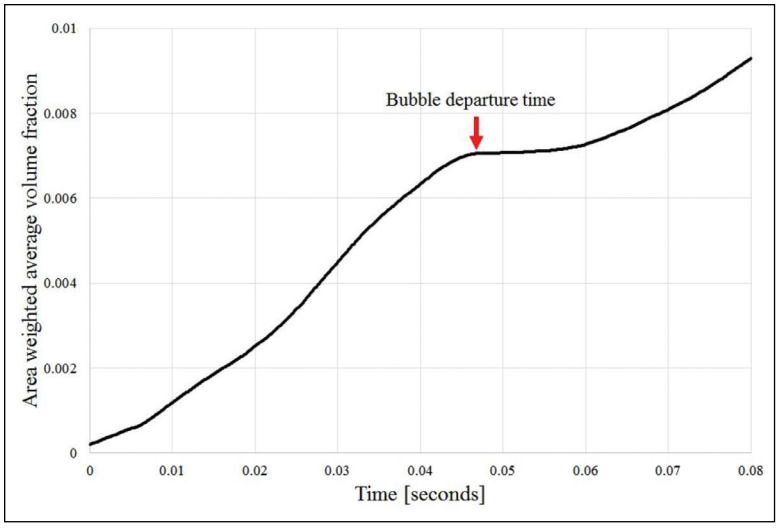

(b)

FIGURE 5
Numerical results of case 9 (no vibration, 60° bubble contact angle). (a) Volume fraction, velocity vector, pressure contour, and temperature profile of case 9 (no vibration, 60° bubble contact angle), (b) Area weighted average volume fraction vs. time.

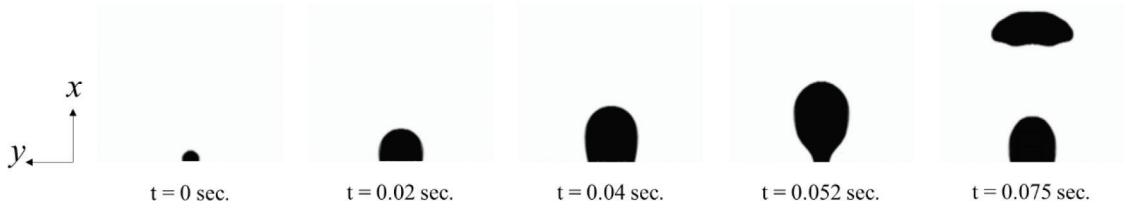

FIGURE 6
The bubble dynamics (case 5: no vibration, 80° bubble contact angle).

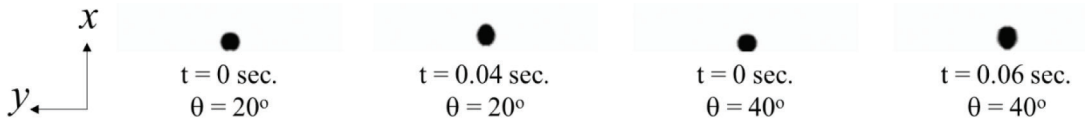

FIGURE 7
The bubble dynamics (case 7 & 8: no vibration, 20° and 40° bubble contact angle).

Effect of Vibration on Bubble Growth

In general, the results show that vibration does not affect the dynamic growth behavior of the bubble, but it does alter both the bubble departure diameter and the bubble departure time. The solver becomes unstable and diverges at 10 to 20 time steps after bubble departure. This solver instability is inconsequential considering that the heat transfer between the bulk fluid and the bubble after departure is insignificant compared to that while the bubble is attached to the wall.

Figure 8 shows the influence of vibration on the detached bubble behavior, including induced surface waves on the liquid-vapor interface. These figures show results immediately prior to the solver divergence. The waves on the bubble surface are not apparent prior to bubble departure ($t = 0.043$ s) because the bubble surface is stabilized by surface tension forces. After the bubble detachment, the bubble interfacial waves propagate from the bubble tail ($t = 0.044$ s) to the top of the bubble ($t = 0.045$ s). This can be explained by examining the velocity field. The velocity scale of case 10 is three times larger than that of case 9 for no vibration. This strong velocity gradient leads to the divergence of the solver. It should be noted that the velocity vector and pressure contour profile of the case 10 in Fig. 8 are not from acceptable converged results. It is presented to illustrate how the solver diverges after the bubble detaches for vibration cases.

The influence of the vibration frequency and the initial vibration direction on the bubble departure diameter, the bubble departure time, and the heat transfer coefficient are illustrated in Fig. 9. The vibration displacement is set to 50 μm for all cases. The results with vibration are normalized by the non-vibration result (case 9). The effect of vibration is apparent in an opposite way to the initial vibration direction. For example, when the initial vibration direction is set as $+x$ (initial phase angle is zero) the normalized bubble departure diameter and the normalized bubble departure time decrease with increasing vibration frequency. The normalized bubble diameter decreases from approximately 1.06 at 5 Hz to approximately 0.92 at 25 Hz. In comparison, Prosperetti (1991) shows that for a vibration frequency of 108 kHz the bubble diameter ratio is approximately 1.07. A decrease in bubble deformation with increasing vibration frequency was also observed by Zawala et al. (2011) for colliding bubbles. In contrast to the $+x$ initial vibration direction condition (case 10, 11, 12), increasing the vibration frequency from 5 Hz to 15 Hz delays the time of bubble departure and augments the bubble size for the $-x$ initial vibration direction (180° initial phase angle) conditions (case 15, 16, 17). Figure 9 shows that vibration does not shorten the bubble departure time for several cases. Even at the same vibration frequency and vibration displacement, the bubble departure diameter and the bubble departure time differ for differing initial vibration directions. However, the individual behaviors cannot be explained

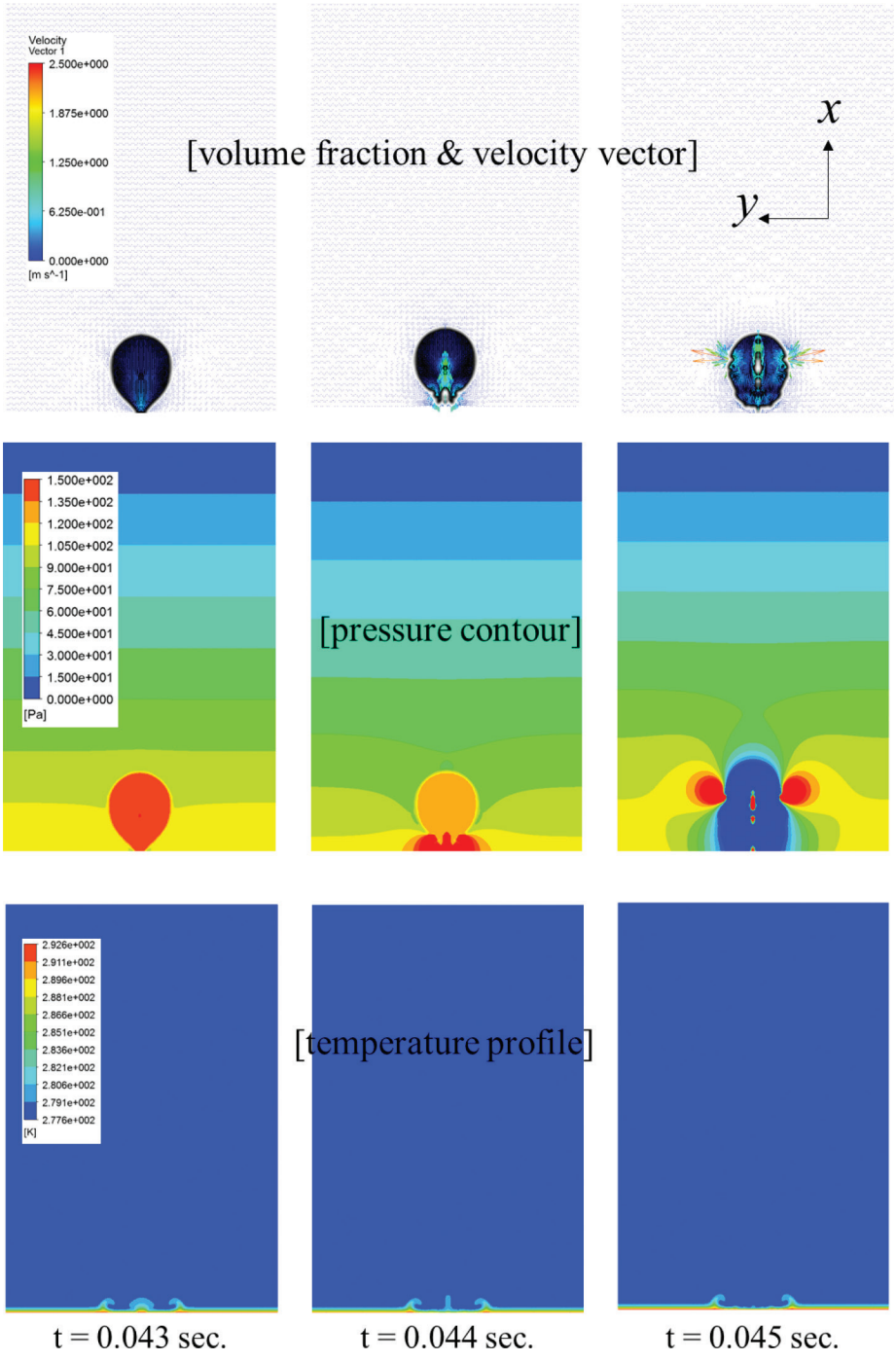

FIGURE 8
Volume fraction, velocity vector, volume fraction, pressure contour, and temperature contour of case 10.

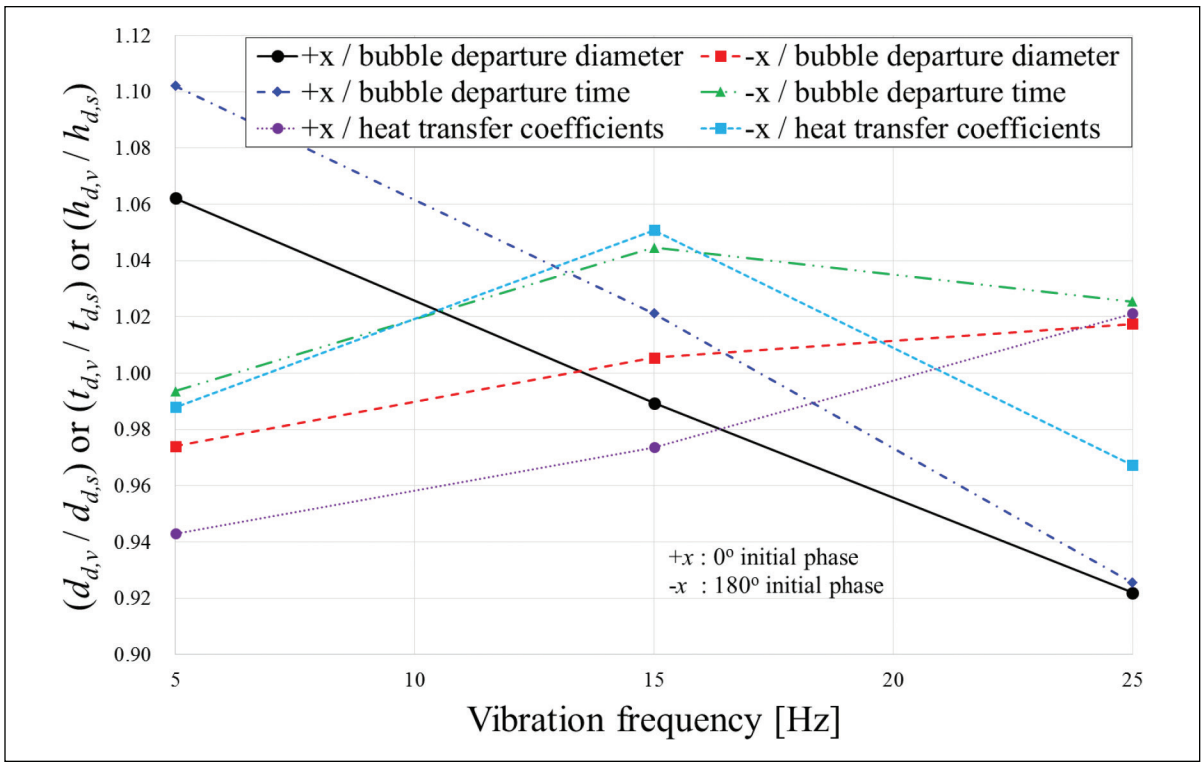

FIGURE 9
The effect of vibration frequency and the initial vibration direction.

only with the sign (direction) of the initial acceleration amplitude.

The effect of vibration displacement is shown in Fig. 10. The vibration frequency and the initial vibration direction (initial phase) are identical for all cases as 25 Hz and $+x$ ($\varphi = 0^o$). At this frequency, all of the cases have smaller bubble departure diameters and shorter bubble departure times than the base case without vibration. Even though the tendency is not linear for the bubble departure time, the effect of the vibration displacement on the basic bubble characteristics is much less than that of the vibration frequency. This is not surprising given that vibration acceleration is proportional to the square of vibration frequency ($a = -A\omega^2 \sin\omega t$).

Effect of vibration on heat transfer coefficients

The heat transfer coefficients ratio (heat transfer coefficients under vibration, $h_{d,v}$ / heat transfer coefficients without vibration, $h_{d,s}$) are shown in Fig. 9 and 10 where $h_{d,v} / h_{d,s} = m_{i,v} / m_{i,s}$. The presented heat transfer coefficients are evaluated at the time of bubble departure. The experimental measured heat transfer coefficient (Kedzierski and Han, 2006), which was measured at the identical operating condition, is much higher (3939 W/m^{2}K) than the presently simulated value (1004 W/m^{2}K) due to the number of active nucleation sites per unit area. The number of active sites of this simulation model is less than 1% of the Benjamin and Balakrishna (1996) model. For this reason the heat transfer coefficients of this numerical work are less than the measured heat transfer coefficients. This study is restricted to single bubble behavior and dynamic inter-related behavior of nearby bubbles/flow field is not considered. Figures 9 and 10 show that there is no clear relationship between either the vibration frequency or the vibration amplitude and the heat transfer coefficients. At the initial zero phase ($+x$ initial moving direction cases), the trend of heat transfer

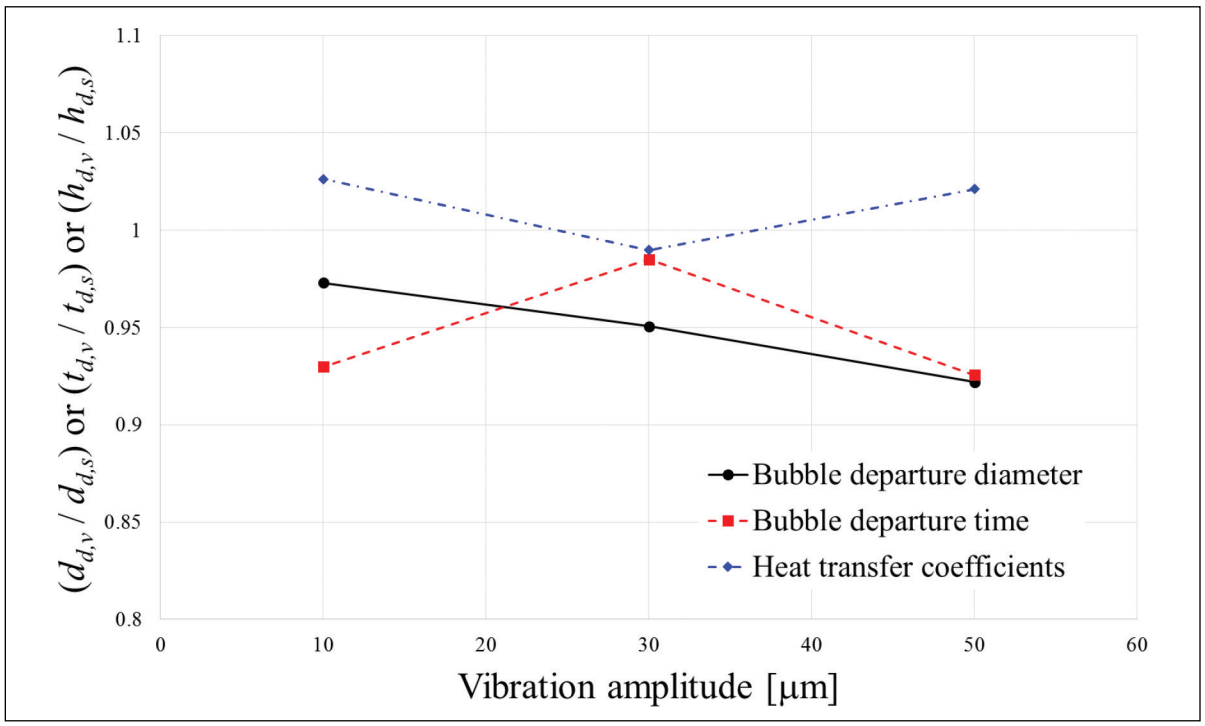

FIGURE 10
The effect of vibration displacement.

coefficients shows the mirror image of the bubble departure time with respect to the vibration amplitude. For the cases of 180° initial phase ($-x$ initial moving direction cases), the heat transfer coefficient has a maximum with respect to vibration frequency. Conversely, for the zero phase case, the heat transfer is shown to increase with respect to vibration frequency. In general, the effect of vibration amplitude and frequency on the heat transfer coefficient is small for the cases studied here. This is consistent with the findings of Park and Bergles (1988) who found that a vibration frequency of 55 Hz had nearly no effect on the heat transfer for low heat flux. The low heat flux condition is presumably a close representation of single bubble performance.

FUTURE WORK

It should be noted that this simulation study has several limitations. Cavitation is not considered because of the low frequency range, but cavitation plays a major role in heat transfer enhancement using the ultrasonic acoustic vibration method. Another major limitation of this phase change modeling is the applicability to a lubricant-refrigerant mixture. In a refrigerant-lubricant mixture, the refrigerant is more volatile and this creates a lubricant rich layer near the heated wall and the vapor bubble. Coupled with temperature dependent properties, especially surface tension, the Marangoni effect may play an important role in the bubble dynamics in refrigerant-lubricant mixtures near the heated wall. Another ignored impact of the presence of a lubricant is foaming. Foaming has several effects: increasing the vapor-liquid interface area, blocking the liquid flow, and enhancing the dynamic interaction when foams burst. This simulation is restricted to single bubble dynamic behavior and interactions with nearby nucleation sites are ignored. It is expected that the magnitude of the bubble parameters would vary for different saturation temperatures due to the change of thermophysical properties and the resulting effect on the force

balance between the buoyancy and the surface tension forces. However, the relative influence of the vibration on the general boiling behavior is expected to remain consistent with the present results. The lack of experimental measurements for single bubbles as influenced by vibration makes it difficult to verify the vibration effects that were illustrated in this paper. Finally, only vibration directions aligned with gravity are considered. Vibrations in directions differing from gravity and the axis of bubble growth are likely to lead to results that differ from those presented here.

CONCLUSIONS

This study illustrates that key bubble parameters are affected by vibration. The low frequency vibration effect on the bubble departure diameter and the bubble departure time in the pool boiling regime was analyzed with the assistance of computational fluid dynamic modeling using the volume of fluid method. The dynamic behavior of bubble growth of R123 at 15 K wall superheat was illustrated with the volume of fraction, the pressure contour, the velocity vector, and the temperature profiles. Vibration increased the bubble contact angle as a consequence of enhanced bubble detachment. The larger bubble dynamic contact angles, in turn, influenced the dynamic shape of the bubble. Low frequency vibrations affect the bubble departure diameter and the bubble departure time. These values can vary with the initial vibration direction resulting in the bubble detachment being promoted or hindered by the low frequency vibration. The vibration impact is augmented with the vibration displacement. Finally, the heat transfer coefficient is strongly related to the bubble departure time rather than the bubble departure diameter. More experimental work is required to verify the influence of vibration on all of the bubble parameters.

ACKNOWLEDGEMENTS

Thanks go to the following NIST staff for their constructive criticisms of the first draft of the manuscript and their helpful discussions: A. Pertzborn, and P. Domanski. In addition, the comments of Y. Kim of Samsung are greatly appreciated.

NOMENCLATURE

A	vibration displacement [m]
A_b	surface area of bubble [m^2]
c_p	specific heat [$J \cdot kg^{-1} \cdot K^{-1}$]
d_b	bubble diameter [m]
d_b	bubble departure diameter [m]
f	frequency [s^{-1}]
F	Source term [$kg \cdot m^{-2} \cdot s^{-2}$]
g	gravitational acceleration [$m \cdot s^{-2}$]
h	heat transfer coefficients [$W \cdot m^2 \cdot K^{-1}$]
i	enthalpy [$J \cdot kg^{-1}$]
i_{lg}	latent enthalpy [$J \cdot kg^{-1}$]
Ja	Jacob number [−]
k	thermal conductivity [$W \cdot m^{-1} \cdot K^{-1}$]
K_l	correlation parameter [−]
L	characteristic length [m]
$\dot{m}_i$	interfacial mass transfer rate per volume [$kg \cdot m^{-3} \cdot s^{-1}$]
p	pressure [$N \cdot m^{-2}$]
Pr	Prandtl number [−]
S	contact length [m]
S_h	Source term [$W \cdot m^{-3}$]
S_ϕ	Source term of ϕ
t_d	bubble departure time scale [s]
t	time [s]
T	temperature [K]
$\vec{u}$	fluid velocity [$m \cdot s^{-1}$]
$\vec{u}_m$	mesh velocity of the moving mesh [$m \cdot s^{-1}$]
v	vibrational velocity [m/s]
V	fluid velocity [$m \cdot s^{-1}$] or volume [m^3]
We	Weber number [−]

Greek Symbols

α	void fraction [−]
Δ	difference [−]
ϕ	variables
Φ	correlation term [−]
Γ	diffusion coefficients
φ	Initial phase [radian]
λ	the most dangerous two-dimensional Tayler inviscid wave length [m]
μ	viscosity [$kg \cdot m^{-1} \cdot s^{-1}$]
Π	fluid property
θ	contact angle [radian]
ρ	density [$kg \cdot m^{-3}$]

σ	surface tension [N·m^{-1}]
ω	angular frequency [radian·s^{-1}]

Subscripts

d	departure
liq	liquid phase
ref	refrigerant
pre	predicted
s	stable
sat	saturation
sim	simulated
v	vibration, vapor
wall	wall
i	liquid-vapor interface

REFERENCES

1. Benjamin, R. J., Balakrishna, A. R. (1996). Nucleate pool boiling heat transfer of pure liquids at low to moderate heat fluxes. Int. J. Heat Mass Transfer. **39**, 2495–2500.
2. Brackbill, J. U., Kothe, D. B., Zemach, C. (1992). A Continuum Method for Modeling Surface Tension. J. Comput. Phys. **100**, 335–354.
3. Carey, V. P. (1992). Liquid-Vapor phase change phenomena: An introduction to the thermophysics of vaporization and condensation processes in heat transfer equipment (2nd edition). Hebron: Tayler & Francis.
4. Esmaeeli A., Tryggvason, G. (2004a). Computations of film boiling. Part I: numerical method. Int. J. Heat Mass Transfer. **47**, 5451–5461.
5. Esmaeeli A., Tryggvason, G. (2004b). Computations of film boiling. Part II: multi-mode film boiling. Int. J. Heat Mass Transfer. **47**, 5463–5476.
6. Ferzieger, J., Peric, M. (1996). *Computational Methods for Fluid Dynamics* (3rd edition). Heidelberg: Springer-Verlag.
7. Fluent User's Guide. (2011). release 14. Ansys Inc. USA.
8. Hou, Y., Hao, D., Shen, C., Shao, Z. (2013). Experimental investigation of the steady-state efficiency of fuel cell stack under strengthened road vibrating condition. Int. J. Hydrogen Energy. **38**, 3767–3772.
9. Hunaidi, O. (2000) Traffic vibrations in buildings. Construction Technology Update. **39**, 1–6.
10. Issa, R. (1985). Soulution of Implicitly discretized fluid flow equations by operator splitting. *J. Comut. Phys. 62*, 40–65.
11. Kedzierski, M. A., Fick, S. E. (2014) Effect of Acoustic Excitation on R134a/Al2O3 Nanolubricant Mixture Boiling on a Reentrant Cavity Surface with Extensive Measurement and Analysis Details. NISTIR 1836, U.S. Department of Commerce, Washington.
12. Kedzierski, M. A., Han, D. H. (2006). Influence of Additives and Concentration of R123/Paraffinic Mineral Oil Pool Boiling Heat Transfer. NISTIR 7336. U.S. Department of Commerce, Washington.
13. Kedzierski, M. A. (1993). Simultaneous Visual and Calorimetric Measurements of R11, R123, and R123/Alkylbenzene Nucleate Flow Boiling. Heat Transfer with Alternative Refrigerants, HTD-Vol. 243, H. J. Sauer, Jr., and T. H. Kuehn, Eds., ASME, New York, pp. 27–33.
14. Kutateladze, S. S., Gogonin, I. I. (1979). Growth rate and detachment diameter of a vapour bubble in free convection boiling of a saturated liquid. High Temperature. **17**, 667–671.
15. Legay, M., Gondrexon, N., Person, S. L, Boldo, P., Bontemps, A. (2011). Enhancement of heat transfer by ultrasound: Review and recent advances, Article ID 670108.
16. Leonard, B., Mokhatari, S., (1990). ULTRA-SHARP Nonoscillatory convection schemes for high-speed steady multidimensional flow. NASATM1-2568 (ICOMP-90-12), NASA Lewis Research Center.
17. McHale, J. P., Garimella, S. V. (2010) Bubble nucleation characteristics in pool boiling of a wetting liquid on smooth and rough surfaces. Int. J. Multiphase flow. **36**, 249–260.
18. Park K. A., and Bergles, A. E., 1988, "Ultrasonic Enhancement of Saturated and Subcooled Pool Boiling," Int. J. Heat Mass Transfer, Vol. 31, No. 3, pp. 664–667.
19. Peyret, R. (1996). *Handbook of Computational Fluid Mechanics* (1st edition). San Diego: Academic Press.
20. Prisniakov, K. V., Nikolaenko, Y. E., Prisniakov, V. F. (2002). Vibration actions on heat pipes as cooling element of electronic systems. Proceedings of the THERMES conference, Santa Fe, New Mexico, USA, January 13–16.
21. Prisniakov, V. F., Prisniakov, K. V. (1997). The physics of heat transfer in boiling and condensation, Proceedings of international symposium on the physics of heat transfer in boiling and condensation, Moscow, Russia, May 21–24.
22. Prosperetti, A., 1991, "The thermal behaviour of oscillating gas bubbles," J. Fluid Mech., i d . 222, pp. 337–616.
23. Prosperetti, A., Crum, L. A., Commander, K. W. (1988) Nonlinear bubble dynamics. J. Acoust. Soc. Am. **83**, 502–513.
24. Riley, N. (1998). Acoustic Streaming. Theoret. Comput. Fluid Dynamics. **10**, 349–356.
25. Son, G., Dhir, V. K. (2008). Three-dimensional simulation of saturated film boiling on a horizontal cylinder. Int. J. Heat Mass Transfer. **51**, 1156–1167.
26. Sun, D., Xu, J., Wang, L. (2012). Development of a vapor-liquid phase change model for volume-of-fluid method in FLUENT. Int. Communications in Heat and Mass Transfer. **39**, 1101–1106.
27. Sung, S. J. (2007). Noise and Vibration (1st edition). Paju: Cheong-Moon-Gak.
28. Turkel, E., Vatsa, V. (2003). Choice of variables and preconditioning for time dependent problems. *16th AIAA Computational Fluid Dynamics Conference, Technical Report AIAA-2003-3692*, June 2003, Orlando, USA.
29. Welch, S. W. J, Wilson, J. (2000). A volume of fluid based method for fluid flows with phase change. J. Computational Physics. **160**, 662–682.
30. Zawala, J., Dorbolo, S., Terwagne, D., Vandewalle, N., and Malysa, K., 2011, "Bouncing bubble on a liquid/gas interface resting or vibrating," Soft Matter, **7**, 6719–6726.
31. Zuber, N. (1959). Hydrodynamic aspects of boiling heat transfer. Ph.D. thesis. UCLA. USAEC Report AECU-4439.